Materials Science & Engineering A 826 (2021) 141978

Contents lists available at ScienceDirect

Materials Science & Engineering A

journal homepage: www.elsevier.com/locate/msea

Dynamic fracture behavior of additively manufactured Scalmalloy®: Effects of build orientation, heat-treatment and loading-rate

John P. Isaac [a], Seungjong Lee [a,b], Nima Shamsaei [a,b], Hareesh V. Tippur [a,*]

[a] Department of Mechanical Engineering, Auburn University, AL, 36849, USA
[b] National Center for Additive Manufacturing Excellence (NCAME), Auburn University, AL, 36849, USA

ARTICLE INFO

Keywords:
Aluminum alloy
Additive manufacturing
Fracture mechanics
High strain-rate fracture
Digital image correlation

ABSTRACT

Scalmalloy® specimens are fabricated using Laser Beam Powder Bed Fusion to investigate the role of build orientation, loading-rate, and heat-treatment on critical energy release rate and crack growth resistance behaviors. Four build orientations - horizontal, vertical, flat, and diagonal - are assessed under dynamic loading conditions. The experiments are carried out in a split-Hopkinson pressure bar apparatus on edge-notched three-point bend geometries. The specimens with the horizontal build are studied also under quasi-static loading conditions to gain some insight into strain-rate sensitivity. The horizontal and flat build specimens are heat-treated for dynamic tests to study the effect of heat-treatment on high strain-rate fracture performance. The in-plane surface displacements near the crack are directly measured using Digital Image Correlation and ultrahigh-speed photography to evaluate the fracture parameters in each of these cases. A hybrid experimental-numerical approach that combines DIC measurements with finite elements is employed to evaluate the fracture behavior. The differences in the critical energy release rates and post-initiation fracture behaviors of Scalmalloy® under different conditions are quantified. The diagonal and horizontal builds outperform the vertical and flat builds in terms of dynamic crack initiation and growth characteristics. The quasi-static crack initiation and growth of the horizontal build specimens show significant strain-rate sensitivity relative to the dynamic counterparts. The heat-treatment of specimens result in marginal improvement of the dynamic fracture performance but does not affect the crack growth resistance behavior. Based on microstructural analyses, the melt-pool boundary orientation relative to crack front extension direction correlates well with the measured dynamic crack initiation and growth performance metrics.

1. Introduction

Additive Manufacturing (AM) in general and metal AM in particular has seen tremendous growth in the past decade or so. The ability of AM to fabricate net shaped parts with intricate features and complex geometries on demand has distinguished it from legacy approaches. Recently, the additively manufactured (AM) metallic parts are beginning to find their way into aerospace, automotive and bio-medical applications where there is an additional need for lightweight and high-performance components. For AM parts to be employed in safety critical applications, new AM material systems which offer superior mechanical properties are also needed. Scalmalloy®, a new aluminum alloy developed by APWorks, is specifically designed for AM to produce a high strength, high ductility, and corrosion resistant alloy with good processability [1]. It is an aluminum-magnesium-scandium alloy, which has the lightness of other Al alloys such as AlSi10Mg with the strength and ductility similar to that of Ti–6Al–4V. These performance characteristics of Scalmalloy® are attributed to its unique microstructure featuring regions of ultrafine grains and fine grains interspersed with each other [2–4]. Magnesium present in Scalmalloy® contributes to its yield strength and also improves the corrosion resistance [5]. The addition of scandium and zirconium is said to be largely responsible for grain refinement and improved mechanical behavior [6–9]. Furthermore, during the AM process, zirconium slows down the coarsening of Al_3Sc precipitates and stabilizes the precipitate morphology which ultimately results in further refinement of the microstructure [10]. This makes Scalmalloy® an ideal material system to be fabricated through AM.

Abbreviations: AM, Additive Manufacturing/Additively Manufactured; LB-PBF, Laser Beam Powder Bed Fusion; DIC, Digital Image Correlation; FE, Finite Element; SEM, Scanning Electron Microscope/Microscopy; EBSD, Electron Back Scatter Diffraction; NHT, Non Heat-Treated; ROI, Region of Interest.

* Corresponding author.
E-mail address: tippuhv@auburn.edu (H.V. Tippur).

https://doi.org/10.1016/j.msea.2021.141978
Received 14 June 2021; Received in revised form 21 August 2021; Accepted 23 August 2021
Available online 24 August 2021

Nomenclature

u	Crack opening displacement
v	Crack sliding displacement
E	Modulus of Elasticity
ν	Poisson's ratio
J	Energy release rate
a	Crack length
u_r	Radial displacement
u_θ	Hoop displacement
XYZ	Build-plate coordinate system
xyz	Crack-tip coordinate system

Table 1
Process parameters used in EOS M290 to print specimens.

Process Parameters	Values
Laser power	370 W
Laser scanning speed	1000 mm/s
Hatching distance	0.10 mm
Layer Thickness	0.03 mm

Table 2
The chemical composition of Scalmalloy®.

Al	Cu	Fe	Mg	Mn	O	Sc	Si	Zr
Bal	<0.1	0.10	4.60	0.50	0.04	0.70	0.20	0.30

However, before AM Scalmalloy® parts are used in fracture-critical applications, their mechanical performance in general and crack initiation and growth behaviors in particular need to be well understood.

A comparative study of mechanical strength of Scalmalloy® and AlSi10Mg produced by Laser Beam Powder Bed Fusion (LB-PBF) was conducted by Awd et al. [11], by testing cylindrical dog-bone specimens. Scalmalloy® samples had a tensile strength of 490 MPa while AlSi10Mg counterparts were at 380 MPa. The metallurgical features responsible for strength enhancement was attributed to the precipitation of Al_3Sc on the grain boundaries that improved the strengthening mechanisms in Scalmalloy®. In another study by Spierings et al. [4], the quasi-static tensile strength difference between the horizontal and vertical build orientations was studied along with the effect of process parameters such as input energy density and scan speed. The material hardness after different heat-treatments was explored in this work as well. They reported that there was no significant anisotropy (<5%) in the stress-strain curves between the build orientations at identical process parameters. In the NHT condition, slight dependence of the mechanical properties on the LB-PBF processing parameters was found. Based on the Brinell hardness measurements, they suggested that a heat-treatment procedure with a temperature between 325 °C and 350 °C and a holding time between 4 and 10 h to be optimum for achieving the maximum material strength in Scalmalloy®. The effect of heat-treatment on the tensile behavior of Scalmalloy® was studied under four different strain-rates ranging from 10^{-3}/s to 10^{3}/s by Jakkula et al., [12]. It was found that the ultimate tensile strength increased with strain-rate after heat-treatment while the failure strain decreased. A comparative investigation of the tensile and fatigue properties for four different AM aluminum alloys (LPW AlSi10Mg, EOS AlSi10Mg, Scalmalloy® and QuesTek Al) was carried out by Muhammad et al., [13]. Among the four Al alloys studied, Scalmalloy® was found to have the highest strength and high ductility from the quasi-static tensile tests. From the results of uniaxial fully-reversed strain-controlled fatigue tests, Scalmalloy® also exhibited the highest fatigue resistance. The superior performance of

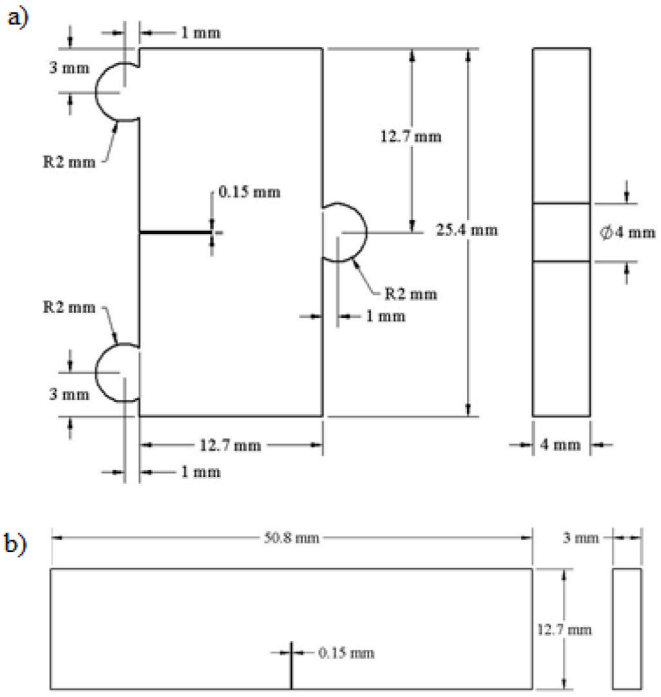

Fig. 2. Test specimen geometries: (a) Dynamic, (b) Quasi-static.

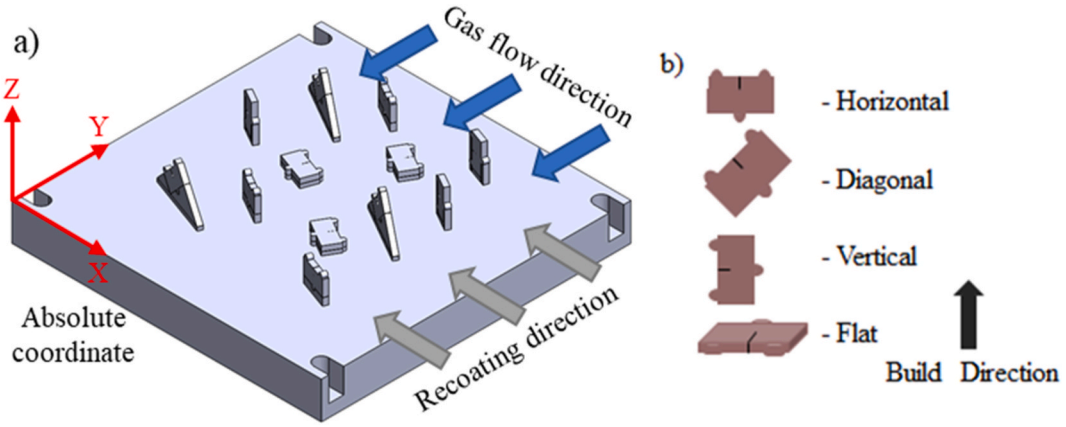

Fig. 1. **(a)** Build plate schematic showing the specimen layout and (b) four different build orientations studied in this work.

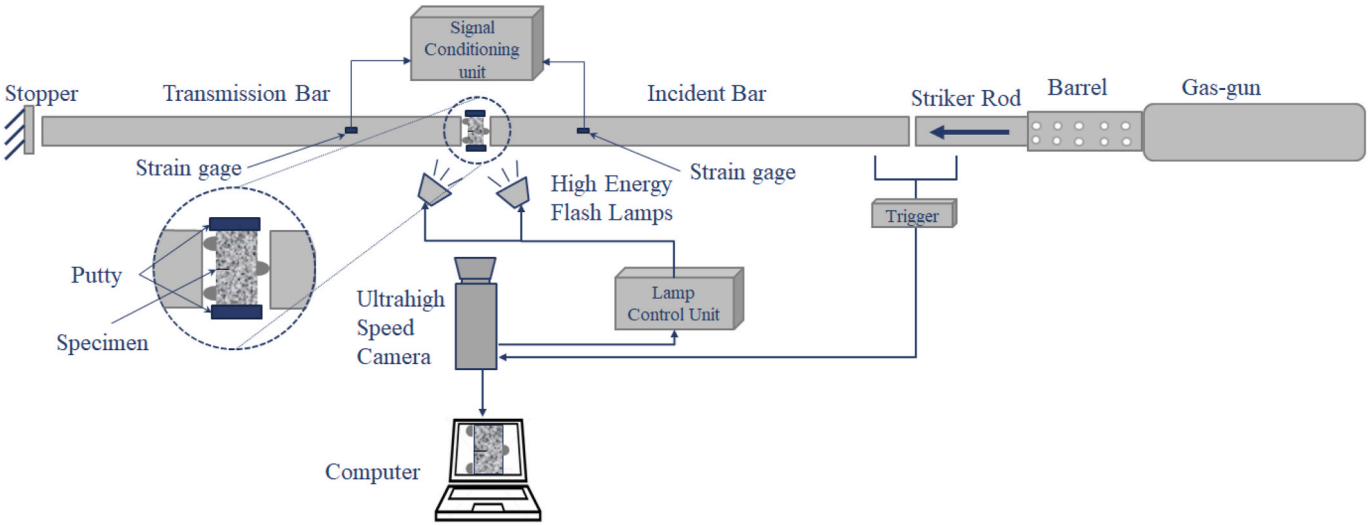

Fig. 3. Split Hopkinson pressure bar apparatus.

Scalmalloy® compared to other AM alloys was attributed to its ultrafine grains.

When it comes to load-bearing, fracture-critical applications, the design and reliability of AM parts using fracture mechanics is important and to authors' knowledge such a report is currently unavailable in the literature. Hence, it is necessary to investigate the effect of factors such as build orientation and post-processing heat-treatment, which could potentially affect the fracture behavior. It is also necessary to study the fracture behavior in the NHT condition [14]. In this paper, the effects of build orientation, loading-rate and heat-treatment on the fracture behavior of Scalmalloy® are considered. Specimens of four different build orientations namely, horizontal, vertical, diagonal and flat are evaluated under high strain-rate loading conditions. The effect of heat-treatment is also examined under high strain-rate conditions but to a limited extent by performing fracture tests on horizontal and flat build specimens. Lastly, the strain-rate sensitivity in the fracture behavior of Scalmalloy® is studied on horizontal build samples under quasi-static loading conditions. All these tasks have been accomplished using a hybrid DIC-finite element (FE) approach to extract the fracture parameters of interest. Earlier approaches based on this concept have involved applying the measured displacements from full-field optical methods as boundary conditions into FE sub-models [15–18]. The particular hybrid methodology employed in this work has been shown previously to capture the fracture parameters with a high degree of fidelity in traditional materials as well as polymeric AM parts under static and dynamic loading conditions [19–21].

In the following, information on Scalmalloy® specimen fabrication is furnished first. This is followed by the details on dynamic experiments, information about the heat-treatment study and then the quasi-static experiments. Subsequently, the results are presented on dynamic fracture tests, effect of heat treatment and quasi-static fracture tests. The microstructural analysis on the fractured specimens follow. The paper concludes with the major findings of the work. A brief explanation of the hybrid DIC-FE method is included in a supplementary document.

2. Experimental details

2.1. Specimen fabrication and geometry

All specimens used in this work were fabricated using an EOS M290, a Laser Beam Powder Bed Fusion (LB-PBF) AM system. The process parameters used for Scalmalloy® are listed in Table 1 [22]. The EOS default scan strategy of 67° scan rotation between successive layers was used for all specimens. To maintain the oxygen level below 1000 ppm during fabrication, argon was used as shielding gas during fabrication. The Scalmalloy® powder used in this work was procured from Carpenter Additive Corp. The chemical composition for the powder is listed in Table 2.

Fig. 1(a) illustrates the build layout used to fabricate Scalmalloy® samples. A square ghost sample, which received no laser power, was also inserted into the top-left corner of the build plate to increase the time interval between the layers. The schematic diagram for the four different build orientations studied in this work under dynamic loading conditions are shown in Fig. 1(b). All sample geometries were modeled using SolidWorks®. After 3D printing, a 6 mm long, 150 μm wide through-the-thickness slit was inserted into 4 mm thick samples using a diamond impregnated circular saw.

The specimen geometry used to perform dynamic fracture tests and quasi-static fracture specimen geometry is shown in Fig. 2(a) and (b) respectively.

2.2. Dynamic fracture tests

The specimen geometry is shown in Fig. 2(a). The pins to load the specimen in a symmetric three-point bend configuration were integrated into the geometry. This approach of integrating the pins to the specimen was preferred over integrating them into the incident and transmitter bars by machining the flat ends of maraging steel due to simplicity. The strategy of performing full-field optical measurements directly on the specimens facilitated this approach even though pins undergo deformation during the loading event. The specimens were sprayed with mists of black and white paint to create random speckles on one of the two surfaces to perform DIC and measure in-plane deformations.

A split-Hopkinson compression pressure bar apparatus was used to subject specimens to rapid stress-wave loading. Fig. 3 shows the schematic diagram of the loading apparatus along with the arrangement for recording speckles during the dynamic loading event. Two C350 maraging steel long-bars of length 2.4 m (96 inches) and diameter 25.4 mm (1 inch) were used as incident and transmission bars. Strain gages were mounted on both the bars to measure the strain history in the respective bars during the loading event. A maraging steel striker rod of length 305 mm (12 inches) and diameter 25.4 mm (1 inch) was propelled from the barrel of a gas-gun to impact the incident bar and generate stress waves. The other end of the incident bar had a flat profile and was in contact with the central loading pin of the specimen. The opposing edge of the specimen with two loading pins was in contact with the flat profile of the transmission bar. All three loading pins were kept in contact with the two long-bars prior to the start of the loading event. In order to hold the

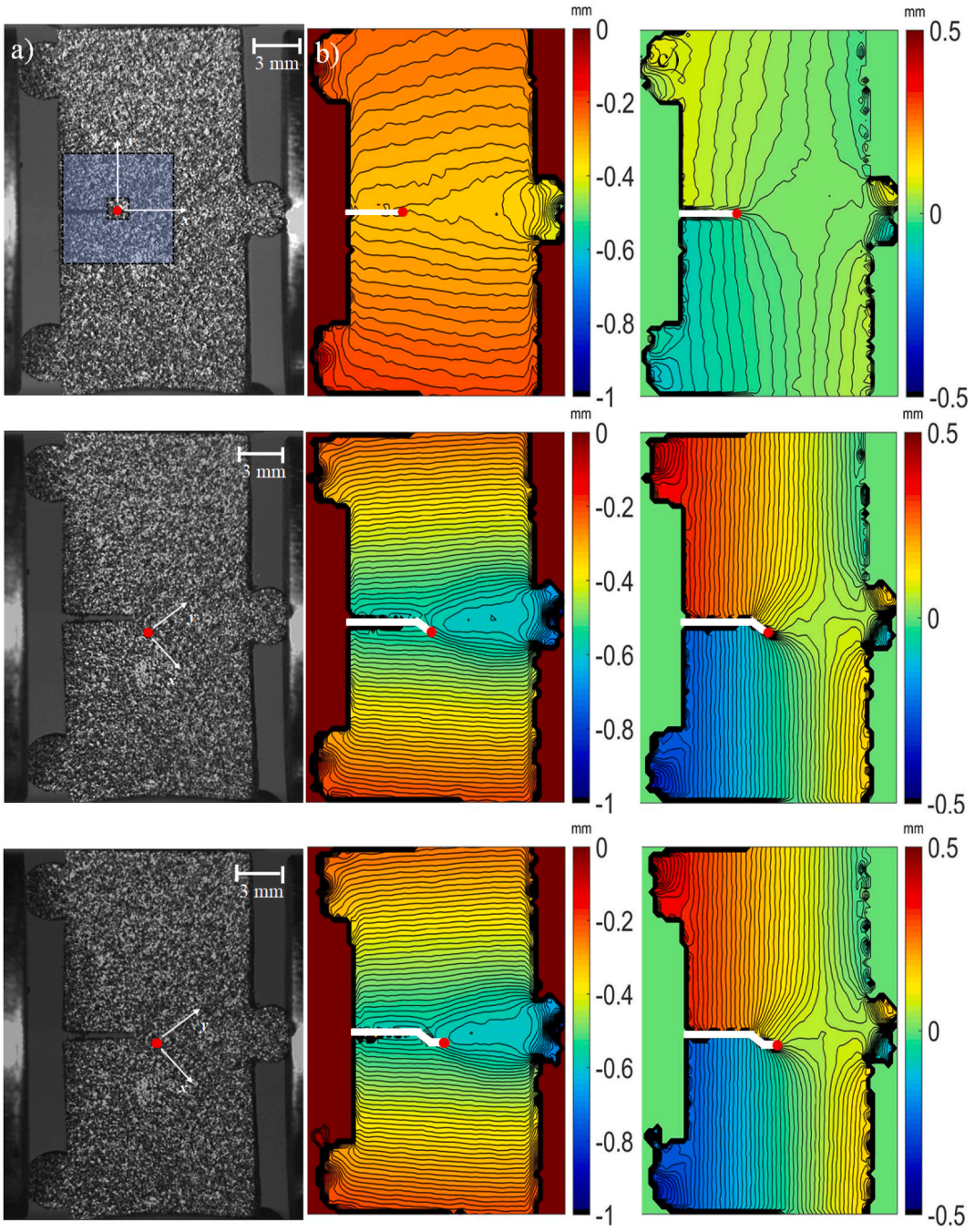

Fig. 4. Optical measurements for a horizontal built specimen: **(a)** Speckle images captured by the camera, **(b)** x- or u-field and **(c)** y-or v-field. Full-field displacement contours are from DIC corresponding to the speckle images, contour interval = 10 μm. First, second and third row corresponds to time $t = -30$ μs, 30 μs and 50 μs respectively ($t = 0$ μs represents crack initiation). Red solid dots indicate the crack-tip position at that particular time instant. (For interpretation of the references to color in this figure legend, the reader is referred to the Web version of this article.)

specimen between the 2 bars from slipping down due to gravity, a block of soft putty was used as a support. Due to the low acoustic impedance of the putty block, an approximately free surface condition was achieved. For acoustic symmetry relative to the loading axis, another putty block was pressed on the top edge of the specimen as well. A Kirana-05 M ultrahigh-speed camera (924 × 768 pixels) fitted with 80–400 mm focal length lens and an adjustable bellows (Nikon PB6) were used to record dynamic deformations at a rate of 200,000 fps. In these experiments, a striker velocity of ~40 m/s was used to impact the specimens to fracture.

2.3. Heat-treatment

The effect of heat-treatment on the dynamic fracture behavior of Scalmalloy® specimens in NHT condition was studied relative to the heat-treated ones. This study was restricted to horizontal and flat build orientations only due to the limited availability of samples. A few horizontal and flat build Scalmalloy® specimens were removed from the build plate and heat-treated to 325 °C for 4 h and furnace cooled to room temperature under Argon atmosphere [4]. All other test procedures used for heat-treated specimens were same as the ones for NHT specimens.

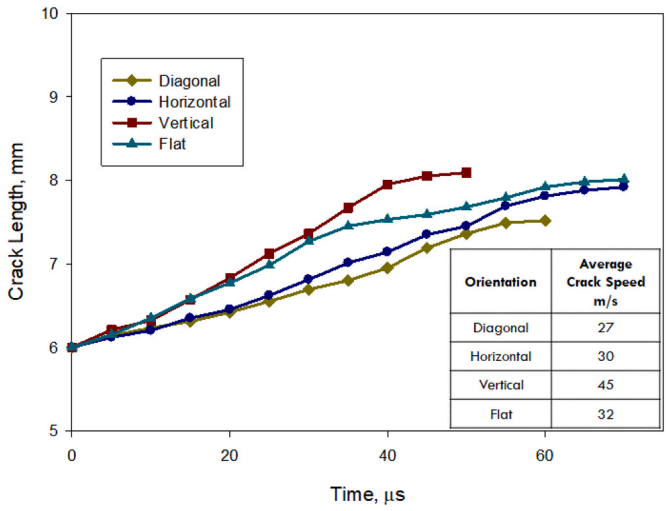

Fig. 5. Crack length histories for edge-notched three-point bend specimens subjected to dynamic loading.

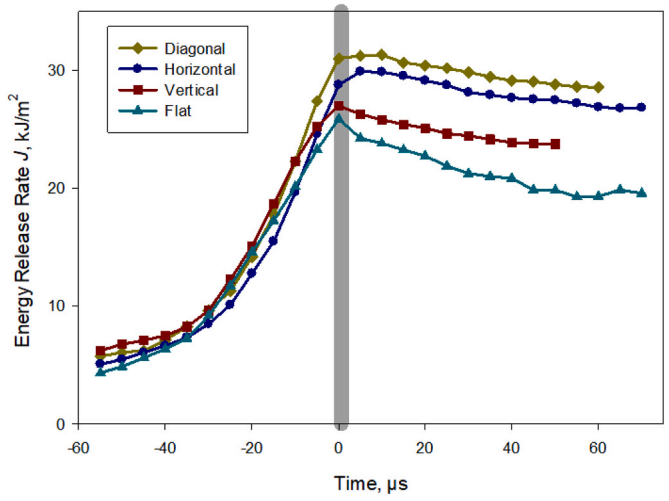

Fig. 6. The *apparent J*-Integral histories for edge-notched three-point bend specimens under dynamic loading condition. Negative and positive times correspond to pre- and post-crack initiation regimes. $t = 0$ corresponds to crack initiation.

2.4. Quasi-static fracture tests

Quasi-static fracture specimen geometry used to study strain-rate effect is shown in Fig. 2(b). The tests were limited again to a single print orientation namely the horizontal build (see, Fig. 1(b)) and the edge-notched symmetric three-point bend specimens were considered. Like its dynamic counterparts, a 150 μm crack of length 5 mm was inserted into the specimen at its mid-span using a circular diamond impregnated saw. An Instron 4465 mechanical loading frame fitted with a 5 kN load cell and roller pin supports of diameter 12.7 mm were used to carry out these experiments at a crosshead speed of 0.005 mm/s. During the tests, load and crosshead displacement histories were recorded. A fine coat of random speckles was sprayed on one of the faces of the specimen in order to perform DIC and quantify in-plane deformations. A PointGrey monochrome camera (2048 × 2048 pixels) fitted with 18–208 mm focal length macro zoom lens recorded the event at a rate of 2 frames per second (fps) or 0.5 s interval from no-load condition to crack initiation and then crack growth until 3 mm.

2.5. Microstructure and fractography

Microstructural characterizations of Scalmalloy® specimens were undertaken to link macroscale measurements with the microscale features. Specimen planes parallel to the *x-z* plane or the crack growth plane (see Section 4.2) were examined. The sectioned samples were first mounted into epoxy and polished using abrasive papers and suspensions to achieve a mirror-like surface finish. The surfaces were then observed in a Keyence VHX-6000 3D optical microscope. Two different light modes were utilized to capture the melt-pool patterns for each build. The microstructure was further observed using a Zeiss Crossbeam 550 scanning electron microscope (SEM). The SEM samples were polished first with a mechanical polisher and then by a vibratory polisher. The SEM images were captured up to 2000× magnification by a backscatter detector. Additionally, the fracture surfaces of the quasi-static and dynamic specimens after failure were photographed using Zeiss Crossbeam 550 SEM.

3. Analysis and results

3.1. Dynamic fracture tests

As described previously, the edge-notched symmetric three-point bend specimens were dynamically loaded (strain-rate ~500 s^{-1}) by impacting the incident bar and then record speckle images during transient fracture event in the specimen with an ultrahigh-speed camera. The strain-rate was measured from the strain gage affixed to the transmission bar. The speckle pattern on the surface of the specimen was photographed during the stress wave loading event at a framing rate of 200,000 fps (or, inter frame duration of 5 μs). The images in the deformed state were correlated.

with the one in the reference (i.e., undeformed) state, recorded before the start of the loading. The speckle images were correlated using ARAMIS® image analysis software. It involved segmenting the images into 25 × 25 pixels sub-images and an overlap of 5 pixels between neighboring sub-images. The scale factor used was ~30 μm/pixel for all dynamic fracture experiments.

Fig. 4 shows select speckle images and the Cartesian displacement contours for the horizontal build orientation. The first row in Fig. 4 corresponds to a time instant before crack initiation. Second and third row corresponds to a time instant after crack initiation. In the first row, the *u*-displacement fields are symmetric relative to the crack and the (horizontal) loading axis. The *v*-displacement field contours, on the other hand, are symmetric in shape and antisymmetric in magnitude relative to the crack. These contours, prior to crack initiation, suggest a dominant mode-I deformation (Fig. 4(a) also highlights the data analysis region.). In the second row of Fig. 4, once the crack initiates, on the surface the propagation occurs at an angle relative to the initial crack orientation. As a result, the local *u*- and *v*-displacement contours are asymmetric relative to the initial and current crack orientations and hence are treated as mixed-mode, mode-I/II fracture. The third row in Fig. 4 represents later stages of crack growth where the crack extends as a mode- I crack after the initial kink. The fracture behavior was similar in all the four build orientations tested and hence for the sake of brevity, the speckle images and displacement contours for the other three build orientations are not provided.

Thus obtained orthogonal displacement component fields were then analyzed using a DIC-based FE approach [19–21] to extract the instantaneous values of energy release rate by computing the *J*-integral. *The details of the methodology can be found in the supplementary materials section of this paper.* During analysis, the material behavior of Scalmalloy® was represented using an elasto-plastic uniaxial stress-strain curve reported in the literature [11]. To further look into the effects of

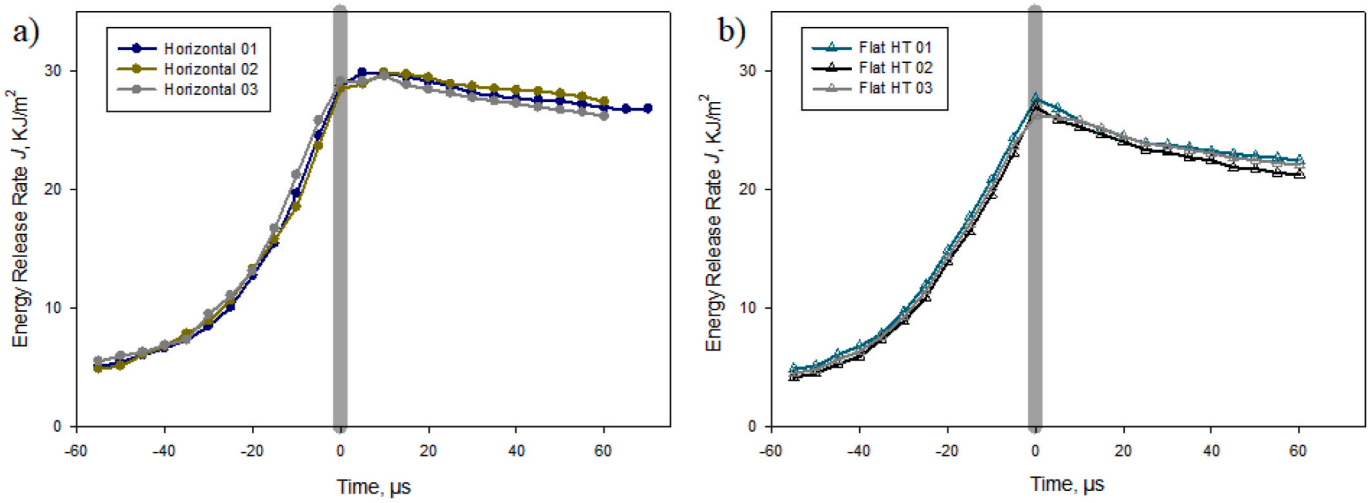

Fig. 7. Repeatability of *apparent* J-integral histories for **(a)** NHT horizontal and **(b)** heat-treated flat built orientation specimens under dynamic loading condition. Negative and positive times correspond to pre- and post-crack initiation regimes. Time $t = 0$ corresponds to crack initiation.

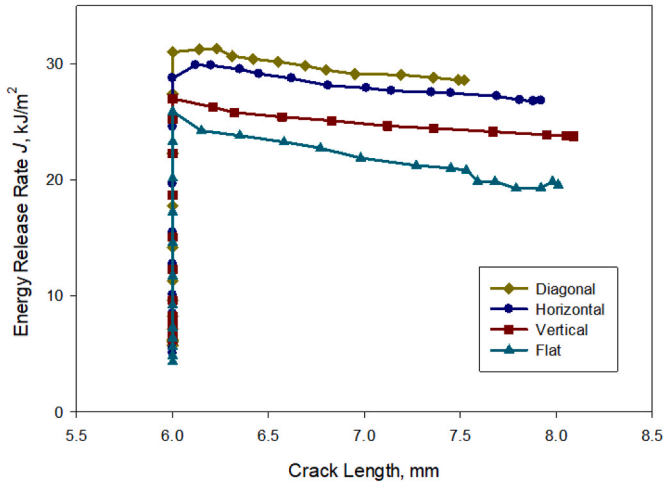

Fig. 8. Apparent crack growth resistance curves for edge-notched three-point bend specimens under dynamic conditions.

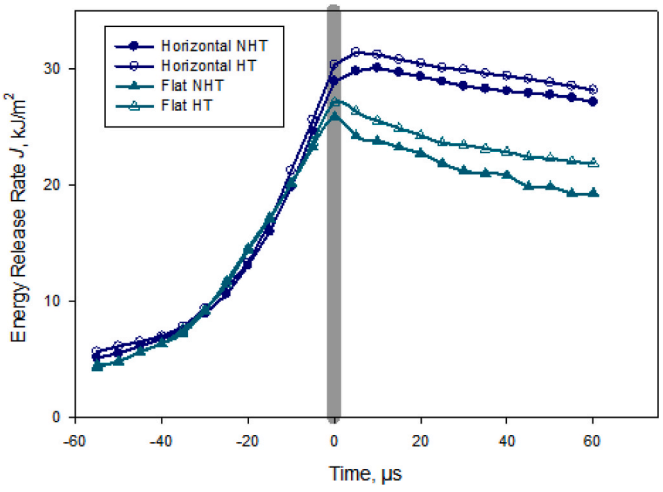

Fig. 9. Comparison of *apparent* J-integral histories for edge-notched three-point bend specimens for heat-treated horizontal and flat builds and NHT counterparts under dynamic loading condition. Negative and positive times correspond to pre- and post-crack initiation regimes. $t = 0$ is crack initiation.

elasto-plastic vs. elastic analyses, the specimen was characterized as an elastic body with $E = 72$ GPa, $\nu = 0.36$ obtained from ultrasonic measurement of longitudinal (6700 m/s) and shear wave (3100 m/s) speeds[1] from the printed specimens to compute the J-integral. It was found that the differences between the two were negligible (see Fig. S4 in the *supplementary materials*).

The crack length histories, obtained by inspecting the speckle images and the crack-tip location where the displacement contours from DIC converge, are plotted in Fig. 5. The crack-tip location was also asserted with the help of transformed displacement fields as needed. This included, plotting radial (u_r) and hoop (u_θ) displacement contours (r and θ being the crack-tip polar coordinates) to aid crack-tip location when

[1] Based on the measured longitudinal wave speed in Scalmalloy® samples, a steady condition is expected to take hold in the specimen after about 15 μs which corresponds to approx. three stress wave round-trips [23,24]. The time duration between the impact and crack initiation being ~85 μs, the data acquired and reported here belongs to the steady state regime. Also, an independent elasto-plastic, dynamic FE explicit simulations (not shown) using SHPB displacement histories as boundary conditions was carried out. Based on the computed kinetic to strain energy ratios, the so-called transition time [25] fell well within 15 μs.

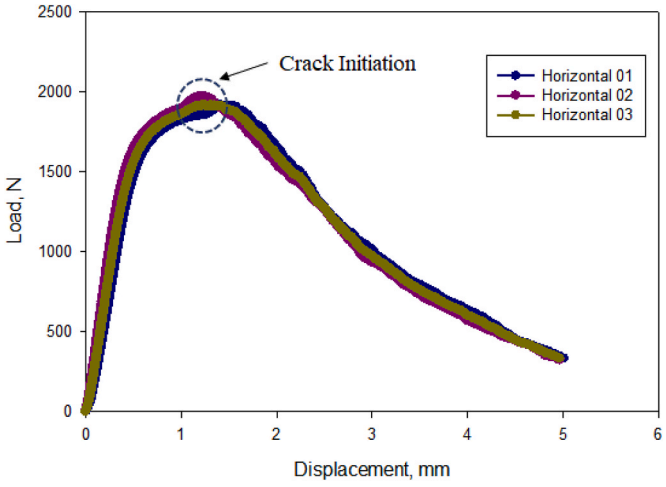

Fig. 10. Load vs. crosshead displacement for the edge-notched three-point bend specimens under quasi-static conditions.

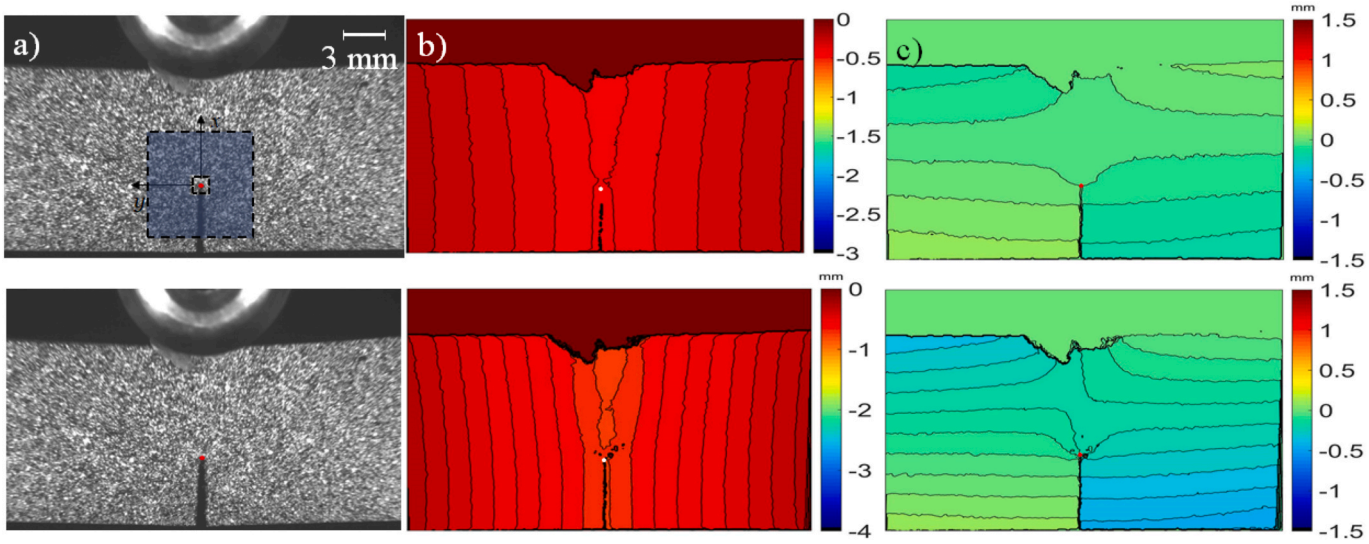

Fig. 11. Surface deformation from quasi-static fracture test: (a) Speckle images at 1050 N and 1860 N. (b) *u*-field, (c) *v*-field displacement contours for horizontal build; contour interval of 50 μm. Red and white solid dots indicate the crack-tip location. The shaded zone in the speckle image corresponds to the region where the *J*-integral is computed. (For interpretation of the references to color in this figure legend, the reader is referred to the Web version of this article.)

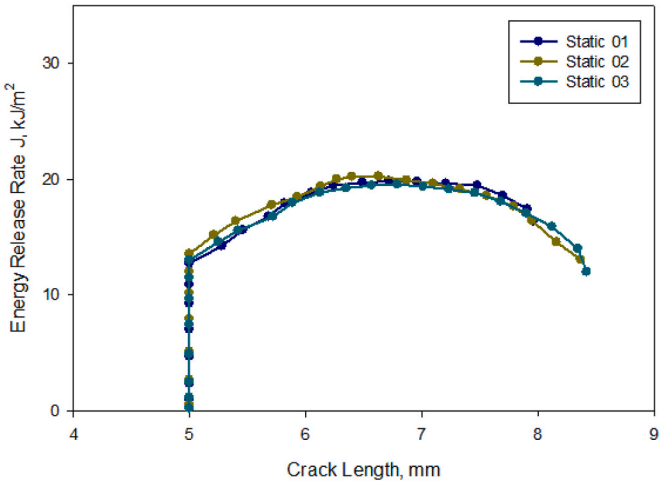

Fig. 12. Apparent crack growth resistance curve for the edge-notched three-point bend specimens under quasi-static loading conditions.

necessary. One such example of u_r and u_θ displacement fields for a dynamically loaded horizontal build specimen is shown in the *supplementary materials* section, Fig. S5. The morphology of contours point to the crack-tip much more clearly than in the traditional displacement components in the traditional Cartesian coordinates. Thus evaluated crack length history suggested the crack growth to be generally monotonic in all the four build orientations. The rates of crack growth were found to be surprisingly low in all the four build orientations. That is, the estimated values were in the range of 30–80 m/s during the observation window, less than 3% relative to the shear wave speeds of ~3100 m/s. Hence, it was reasonable to evaluate the *J*-integral using quasi-static formulations.[2] It should also be noted that due to triaxial effects, the *J*-integral values vary along the 3D crack front in the thickness direction. The objective of this work being comparative evaluation of fracture parameters for different build orientations, the *J*-values from surface measurements can be used. Furthermore, specimens of relatively small thickness allow the usage of plane stress assumptions. *To distinguish these aspects with classical definition, the evaluated J-integral values should be viewed as "apparent" values.*

Fig. 6 shows the histories of the apparent *J*-integral obtained by the DIC-based FE approach for all the builds under dynamic loading conditions. Until crack initiation, as to be expected, the *J*-integral values essentially overlap until crack initiation (or, time $t = 0$) and the.

variations are approximately parabolic in nature. However, the values do show differences at crack initiation and beyond. The apparent *critical* energy release rate or the *J*-integral at crack initiation was the highest for the diagonal build at 31.0 kJ/m^2, followed by the horizontal build at 28.8 kJ/m^2, and then by the vertical build at 27.0 kJ/m^2. The flat build specimens had the least value among all the four at 25.9 kJ/m^2. The crack propagation behaviors of the diagonal and horizontal builds had a similar response. That is, the crack growth was stable with $dJ/da > 0$ immediately after crack initiation ($t = 0$) for a short period of time (15–20 μs), and subsequently, the energy release rate values precipitously dropped, $dJ/da < 0$. In the case of vertical and flat builds, however, the energy release rates dropped ($dJ/da < 0$) soon after crack initiation ($t = 0$). Hence, considering all four responses together, the diagonal build samples were found to be the most favorable with the horizontal build samples a close second and flat build ones were the least desirable.

To ensure the repeatability of these tests and the apparent *J*-integral calculations, a limited number of tests were repeated. Two such results with three different specimens each category are shown in Fig. 7; Fig. 7 (a) for the horizontal build specimens in NHT state and Fig. 7(b) for flat build specimens after heat-treatment. As evident from the results, the *J*-integral histories are highly repeatable for both groups. The scatter in the histories before ($t = -40$) and after ($t = 20$) crack initiation was ~0.1 kJ/m^2 (~2%) and ~0.3 kJ/m^2 (~1%), respectively.

By combining the crack length and the apparent *J*-integral histories, the crack growth resistance behavior for all four build orientations were obtained. Fig. 8 shows the crack growth resistance curves under dynamic loading conditions. In the horizontal and the diagonal builds, crack growth with dJ/da ~0 to mildly positive (or stable growth) was observed after crack initiation for a short range followed by unstable crack growth ($dJ/da < 0$). Flat and vertical builds show unstable crack growth with $dJ/da < 0$ after crack initiation. Other aspects of crack

[2] If the crack were propagating, say, at ~30% of the shear wave speed of the material, as it often does in brittle materials subjected to impact loading, this approach of extracting the energy release rate would not be appropriate as the *J*-Integral is not path independent under transient conditions.

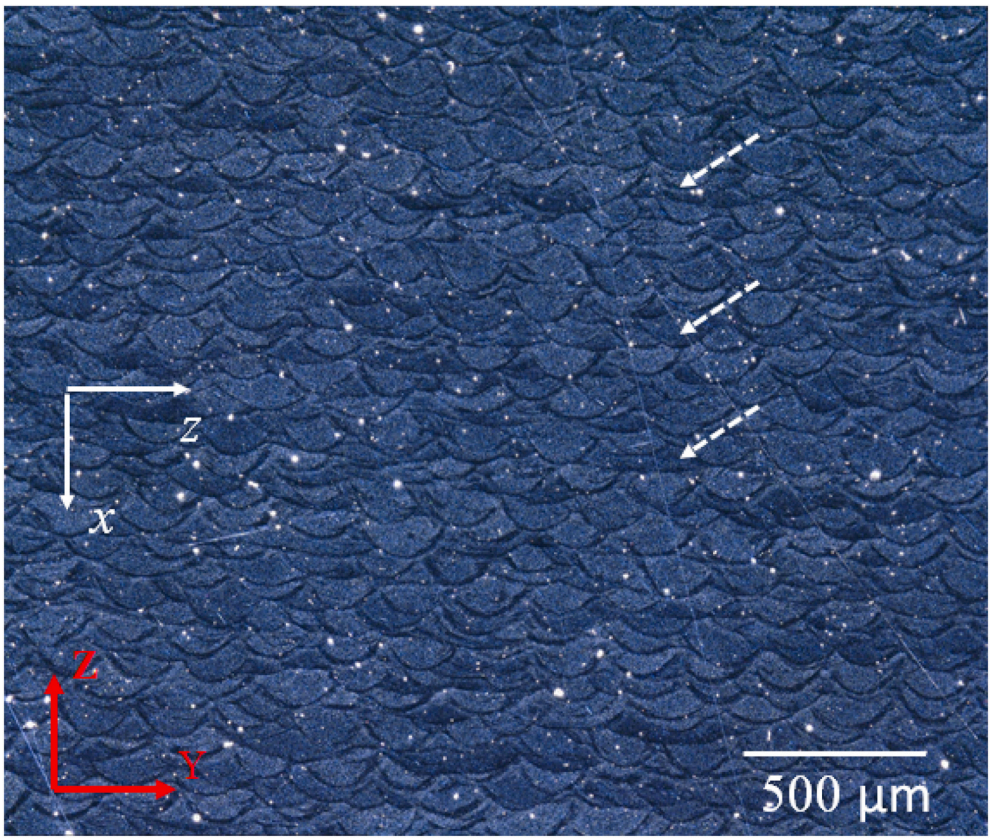

Fig. 13. *x-z* plane (crack-tip coordinate system) images showing scan lines (dotted arrows) and melt-pool structures obtained using optical microscopy for horizontal build orientation. Note: *xyz* represents crack-tip coordinates (in white) and XYZ represents build plate coordinates (in red). (For interpretation of the references to color in this figure legend, the reader is referred to the Web version of this article.)

growth behavior align well with the description provided for Fig. 6.

3.2. Heat-treatment

The dynamic fracture performance results for heat-treated samples are presented next. Due to a limited number of samples available for this study, only the horizontal and flat build orientations were studied. The dynamic fracture tests, again at a strain rate of ~500 s^{-1}, were performed on heat-treated specimens as discussed previously; all other parameters including the ones for DIC described previously was employed. Fig. 9 shows the effect of heat-treatment on the *J*-integral histories for the two flat built and two horizontal built specimens, one of each orientation with and without heat-treatment. Until crack initiation, the responses of NHT and heat-treated specimens essentially overlap on each other. The energy release rate at crack initiation for the heat-treated specimens, however, are higher by approx. 5% in both the horizontal and flat built orientations. More importantly, the overall post-initiation trends approximately parallel the NHT specimens. Thus, by extension, it is reasonable to assume that the effect of heat-treatment on all Scalmalloy® builds, including the vertical and diagonal ones, would marginally increase the dynamic crack initiation toughness. However, the post-initiation crack growth behavior will remain unchanged after heat-treatment. Repeatability for the apparent *J*-integral histories for the heat-treated flat builds under dynamic conditions is shown in Fig. 7(b). The critical energy release rate value for the heat-treated flat build was 27.0 ± 0.7 kJ/m^2.

3.3. Quasi-static fracture tests

The load vs. crosshead displacement plot for the three-point bend test under quasi-static loading (~10^{-4} s^{-1}) condition is shown in Fig. 10 for three horizontal built specimens. The strain-rate was computed from DIC measurements by tracking ε_{yy} at specific sub-image locations near the loading pin for every recorded image until crack initiation. An approx. linear response was seen until about 1700 N of load and there after the response was nonlinear. The distinct perturbation in the load-displacement plot punctuates the crack initiation event close to the peak load. After crack initiation, there was a gradual drop in the load due to ductile crack growth.

Fig. 11(a) shows speckle images before and after crack initiation for the quasi-statically loaded specimen with horizontal build orientation. Fig. 11(b) and (c) show the corresponding *u*- and *v*-displacement contours obtained from DIC. The gray scale photographs of surface speckles (Fig. 11(a)) recorded by the camera in the deformed state were correlated with the reference images recorded in the unloaded state (not shown) to obtain the displacement component fields in two orthogonal directions. As in the dynamic cases, the image analysis software, ARAMIS®, was used to perform gray scale correlation by segmenting images into 25 × 25 pixel sub-images with 5 pixels step size between neighboring sub-images. The scale/magnification factor was ~14 μm/pixel for these images. It should be noted that the displacement data are available as rectangular arrays over the ROI and at the center of each sub-image although they are displayed as contours in these figures after post processing. The constant values from the apparent *J*-integral vs. contour number plot for the static experiments, averaged over contour numbers 14–70 or 1 mm–5 mm (r/B ratio ~ 0.3–1.7; shaded region in Fig. 11(a)), were recovered as the *J*-integral at each load-step.

Fig. 12 shows the variation of energy release rate as a function of crack length for the horizontal build orientation under static loading conditions. It can be seen that the energy release rate after crack initiation continues to increase ($dJ/da > 0$) suggesting a stable crack growth. When compared to its dynamic counterpart, the critical energy release

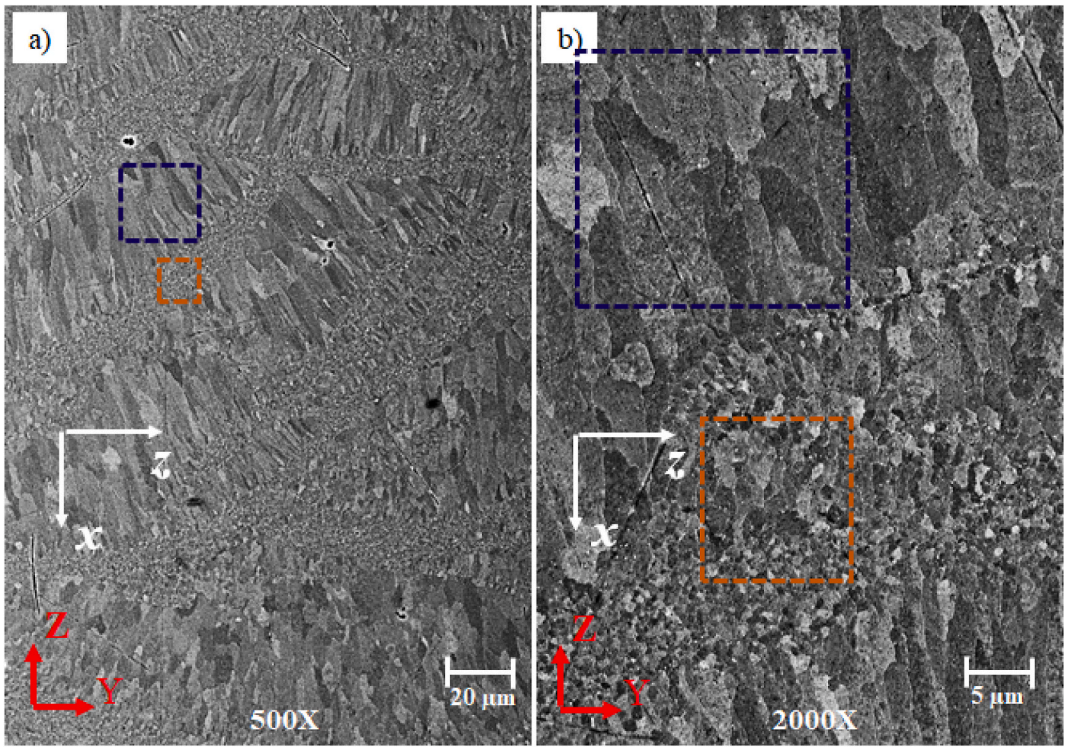

Fig. 14. (a) and **(b)** SEM images of the *x-z* plane (crack-tip coordinates) for the horizontal build orientation at a magnification of 500X and 2000X, respectively. Blue section highlights the regions of columnar grains and orange domains highlight the ultrafine equiaxed grain regions. Note: *xyz* represents crack-tip coordinates (in white) and XYZ represents build plate coordinates (in red). (For interpretation of the references to color in this figure legend, the reader is referred to the Web version of this article.)

rate was about 40% lower under quasi-static conditions at 12.7 ± 0.2 kJ/m^2. This can be attributed to the availability of sufficient time for defects such as pores, lack of fusion zones and inclusions to get mechanically excited and assist in crack initiation. However, the post-initiation regime crack growth involves energy release rate increase to a much higher plateau value of 20.1 kJ/m^2 before becoming unstable ($dJ/da < 0$). It should be noted that these quasi-static experiments with other horizontal built specimens were also repeatable.

4. Discussion

4.1. Effect of build orientation under dynamic conditions

For understanding the differences in macroscale fracture responses among different build orientations under high strain-rate (~500 s^{-1}) conditions, microstructural analysis of Scalmalloy® specimens was carried out. Specimen planes parallel to the one in which the crack propagated namely, the *x-z* plane were investigated. Fig. 13 shows the *x-z* plane images.

obtained for the horizontal build orientation. The scan lines and the melt-pool patterns can be clearly seen in the *x-z* plane image for the horizontal build orientation. The lines which run horizontally in the image and spaced periodically in the vertical direction indicate the scan lines (see, white dotted arrows). The individual melt-pools can be clearly seen along the scan lines/laser path and as expected the melt-pools are periodic and somewhat uniform in structure throughout the *x-z* plane. This minimizes meandering of the crack front into other planes during the growth of the crack front in the *x-z* plane and in the *x*-direction. Similar images of the melt-pools were obtained for the diagonal, vertical and flat build orientations as well; for the sake of brevity, they are not shown here. However, the size, shape and the uniformity of the melt-pools were similar to that for the horizontal build orientation (Fig. 13).

Fig. 14(a) and (b) show example SEM images with the backscatter detector for the horizontal build orientation at two different magnifications. The melt-pool boundaries can be partly observed in Fig. 14 (also see, Fig. 13) on the *x-z* plane for the horizontal build orientation. The grain morphology associated with each melt-pool can be broadly classified into two types, equiaxed finer grains seen along the melt-pool wall or the skin (marked by orange colored domains in Fig. 14(a) and (b)) and larger elongated grains within the melt-pool (marked by dark blue domains in Fig. 14(a) and (b)). Furthermore, the latter ones are approx. normal to the build plate. The regions of ultrafine grains and columnar grains seem interspersed with each other throughout the microstructure. The ultrafine grain regions, with many grains in the submicron range, exist due to the presence of Al_3Sc and Al_3Zr precipitates while the columnar grains are formed from rapid and directional solidification process [26–28]. Similar SEM images for the diagonal, vertical and flat build orientations are also obtained but not shown here for brevity. Again, apart from the directional differences in the columnar grains due to the orientation of specimens on the build plate, no other significant differences were seen. An average grain size of 1.2 μm was determined in the finer grain region and of width of 3–5 μm and length of 40–60 μm were found in the elongated grains region.

To gain further insight into the crack front and microstructure interactions during crack initiation and growth, electron backscatter diffraction (EBSD) images were obtained. Fig. 15 shows those images for the *x-z* plane in all four build orientations considered. The presence of a highly refined submicron sized grains formed because of precipitation hardening makes Scalmalloy® microstructurally complex.

From the EBSD images, a striking variance between the two build orientations having the largest difference in measured macroscale critical fracture parameters is evident. Fig. 15(b) and (d) show the EBSD images for the diagonal and flat build orientations. It can be seen that the ultrafine grains that constitute the melt-pool boundary are approximately perpendicular to the direction of crack growth in the diagonal build whereas the columnar grains are perpendicular to the crack

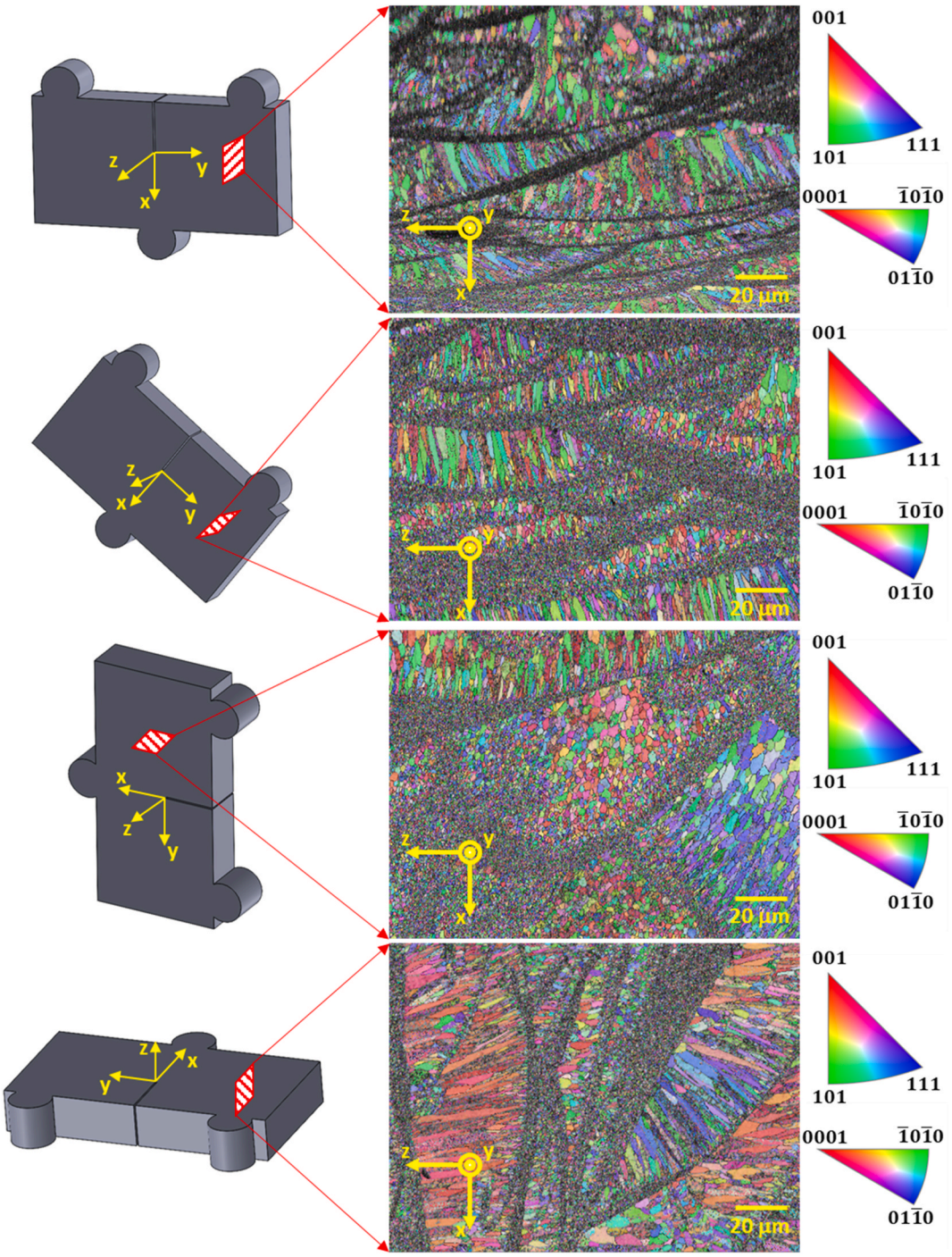

Fig. 15. EBSD images of the *x*-*z* plane for the **(a)** horizontal, **(b)** diagonal, **(c)** vertical and **(d)** flat build orientations. (Only crack-tip coordinates are shown; build plate coordinates XYZ are not shown.)

growth direction in the flat build counterpart. Thus, when the crack initiates and propagates in diagonal specimens, the crack front has to grow past regions of ultrafine grains requiring greater expenditure of energy. In the case of flat build, however, once the crack initiates, it can travel through the columnar grains more easily. This in turn significantly reduces the number of grain boundaries interfering with the crack growth in the flat build. This also explains the crack growth behavior in the diagonal build that showed $dJ/da > 0$ initially under high strain-rate conditions. Further quantitative microstructure analysis was carried out using ImageJ software. For a series of 100 μm long lines along the *x*-axis (crack growth direction) in the EBSD images for the diagonal and flat builds, the average number of grain boundaries penetrated was calculated. In case of the diagonal build approx. 160 grain boundaries were encountered by the prospective crack front whereas for the flat build it was about 90 grain boundaries. This further strengthens the argument put forth earlier to explain the differences in the macroscale fracture responses presented in Fig. 6. Additionally, from Fig. 15(a) and (c) it can be noted that the number of grain boundaries that has to be penetrated by a growing crack (in the *x*-direction) fall between the diagonal and flat build specimens, consistent with the crack growth resistance behaviors seen in Fig. 8.

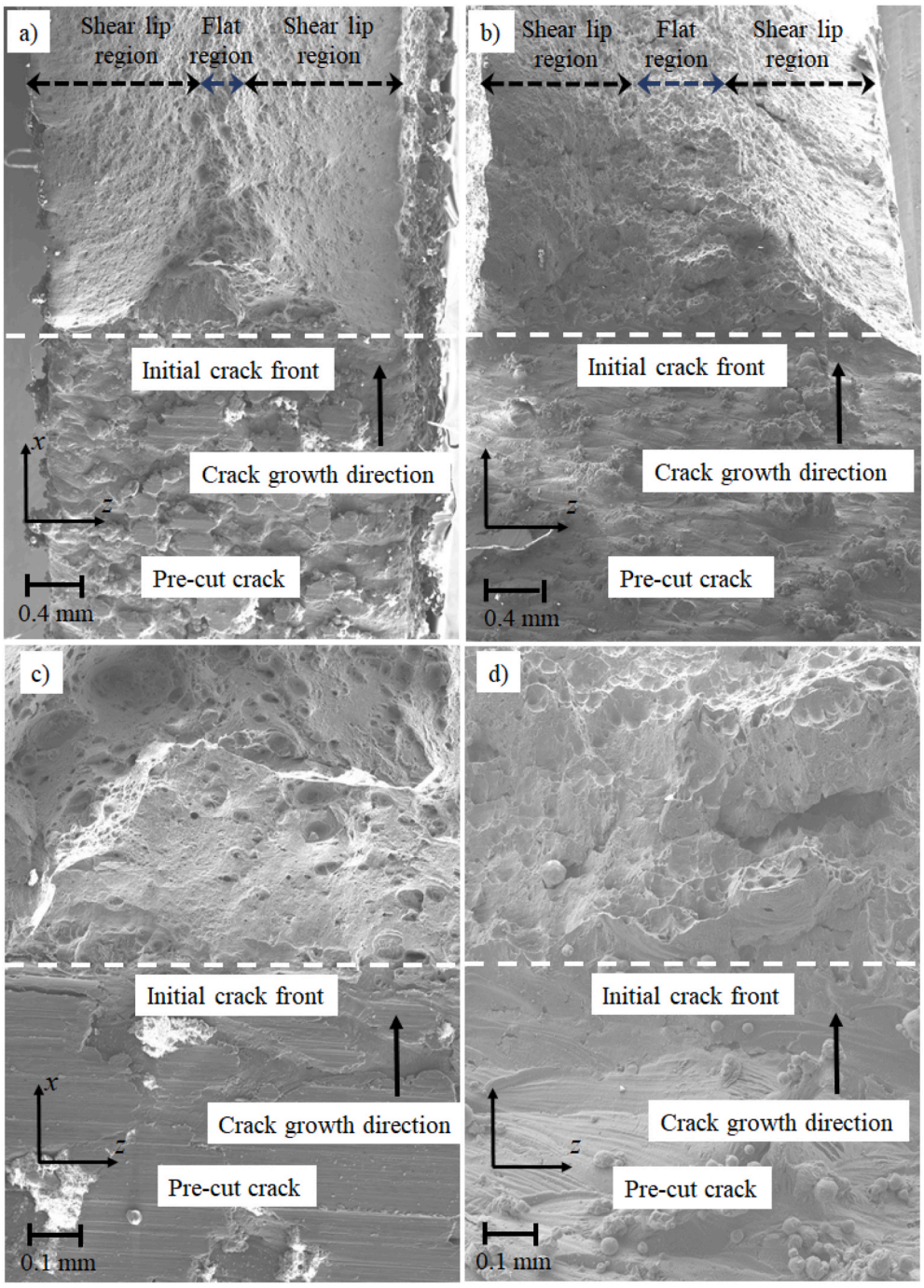

Fig. 16. Fracture surface images of horizontal build orientation obtained by SEM for **(a)** static and **(b)** dynamic specimens at 25X. **(c)** and **(d)** shows the SEM images taken at 100X for static and dynamic specimens respectively.

4.2. Effect of heat-treatment

A temperature of 325 °C used in this study for heat-treatment facilitated grain refinement and formation of fine grained Al_3Sc and Al_3Zr precipitates in Scalmalloy® [4]. The presence of Sc in traditional Al-alloys has previously been found to produce greater precipitation [29,30]. Hence, the increase in the critical energy release rate under dynamic loading conditions for the heat-treated samples can be attributed to the larger number of Al_3Sc and Al_3Zr precipitates. The fracture behavior itself did not produce discernible change due to heat-treatment although the magnitude of energy release rates observed in the crack propagation regime was marginally but consistently higher than NHT counterparts. With heat-treatment, increase in ultimate tensile strength along with decrease in failure strain was reported in literature [12], During fracture, just marginal differences (5%) in the crack initiation was evident in heat-treated samples. This behavior discrepancy between the tensile and fracture samples due to heat-treatment can be accredited to the fact that toughness (area under the nominal stress-nominal strain curve) is approximately unchanged under heat-treatment. Hence, for energy release rate values under fracture tests to exhibit marginal differences is expected.

4.3. Effect of loading-rate

To gain insight into the role of loading rate into differences in the macroscale fracture behaviors, the fracture surfaces of the horizontal build specimens after static ($\sim 10^{-4}$ s^{-1}) and dynamic (~ 500 s^{-1}) three-point bending tests were investigated with Zeiss Crossbeam 550 scanning electron microscope. Fig. 16 shows statically and dynamically fractured specimen surfaces at two different magnifications. The cross-sectional area including the crack initiation region was captured which provides surface elevation data. As marked in Fig. 16(a), (b), distinct regions corresponding to slant and flat fractures are evident in the cross-sectional view adjacent to the free-surfaces and the specimen mid-plane, respectively. In case of the dynamically fractured specimens (Fig. 16(b)), a relatively wider flat fracture region can be seen when compared to the quasi-static counterpart in Fig. 16(a). Quantification of these features in ImageJ software indicates ~10% of the fracture surface was flat under quasi-static conditions whereas it was ~25% in the dynamic case. Hence, the availability of sufficient time for a complete manifestation of microstructural defects and dislocation mobility leading to crack tunneling and shear lips formation distinguishes quasi-static fracture from its dynamic counterpart. Furthermore, the significant slant fracture is attributed to relatively thin samples that introduce significant plane stress behavior adjacent to the specimen surfaces (x-y plane). The higher magnification images (see Fig. 16(c) and (d)) show the dynamic fracture surface to be somewhat more textured than the static counterparts. This may be attributed to higher critical fracture toughness in the former than the latter. These images are taken near the initial crack front on the specimen mid-plane.

5. Conclusions

Dynamic fracture behavior of AM Scalmalloy® specimens were experimentally studied using a split-Hopkinson pressure bar apparatus. Four different build orientations namely, horizontal, diagonal, vertical and flat, were considered for this study and the effect of build orientation under dynamic conditions was investigated. The effect of heat-treatment was also studied in a limited fashion using horizontal and flat build specimens under dynamic loading conditions. The loading-rate effects on the fracture behavior of Scalmalloy® were investigated for the horizontal build orientation by carrying out quasi-static experiments. The optical method of DIC was utilized to map the in-plane orthogonal displacements in the whole field during both static and dynamic experiments. The optically measured crack-tip displacement fields from DIC were imported into corresponding finite element discretization as full-field surface boundary conditions to extract the energy release rate by computing the J-integral using in-built sub-routines in ABAQUS. The validity of the dynamic computations was ensured after approx. three stress wave reverberations in the specimen and a relatively slow crack growth. This experimental-numerical approach was implemented for both static and dynamic experiments to obtain the fracture parameters before and after crack initiation. Further, the microstructures were analyzed to explain the observed macroscale responses. The major conclusions of the work are as follows:

- Under high strain-rate conditions, different *critical* energy release rates and fracture behaviors were observed in all four build orientations. The diagonal build orientation had the highest critical energy release rate at 31.0 kJ/m^2. The performance of the diagonal build was followed by the horizontal, vertical and flat builds, respectively, with the flat build having the lowest critical energy release rate at 25.6 kJ/m^2.
- The diagonal and horizontal builds showed a stable crack growth regime ($dJ/da > 0$) upon initiation, which transitioned to unstable growth ($dJ/da < 0$) subsequently. The vertical and flat builds, however, showed an unstable crack growth right after initiation.
- The differences in the macroscale fracture behavior between the build orientations was explained in terms of the grain morphology along the crack path. The encounter between the crack front and the ultrafine grained melt-pool boundaries seem to contribute to the differences in the crack initiation and growth behaviors among different builds.
- Both horizontal and flat builds showed marginally (~5%) higher critical energy release rates after heat-treatment relative to their NHT counterparts. The overall energy release rate trends, however, was not altered during crack propagation because of the heat-treatment. The grain refinement and formation of larger number of nanometer-sized precipitates were attributed to this slight improvement in the fracture performance.
- The strain-rate effect comparison among horizontal build samples showed significant differences. The *critical* energy release rate under quasi-static conditions was found to be approx. 40% lower than the dynamic counterpart. However, the crack propagation behaviors in the two cases were substantially different with a large stable crack growth region with $dJ/da > 0$ after initiation in the former whereas the same turned unstable in the latter with $dJ/da < 0$ soon after crack initiation. These differences were reflected in significantly different slant vs. flat fracture regions seen in the fractured specimens.

Data availability statement

The original data will be made available by the authors upon request.

CRediT authorship contribution statement

John P. Isaac: Conceptualization, Experiments, Formal analysis, and interpretation, Writing – original draft, and subsequent editing. **Seungjong Lee:** Additive printing, Microstructural analysis, Draft reviewing and editing. **Nima Shamsaei:** Additive printing, Microstructure analysis, Draft reviewing and editing. **Hareesh V. Tippur:** Conceptualization, Experiments, Formal analysis, and interpretation, Writing – original draft, review and editing.

Declaration of competing interest

The authors declare that they have no known financial interests or \npersonal relationships that could influence the work reported in this paper.

Acknowledgments

This material is based upon the work partially supported by the Federal Aviation Administration (FAA) under Cooperative Agreement 12-C-AM-AU. Partial supports from the U.S. Naval Air Systems Command (NAVAIR) and EOS North America Inc. are also acknowledged. Contributions of Mr. Sivareddy Dondeti towards the development of hybrid DIC-FE methodology are gratefully acknowledged.

Appendix A. Supplementary data

Supplementary data to this article can be found online at https://doi.org/10.1016/j.msea.2021.141978.

References

[1] K. Schmidtke, F. Palm, A. Hawkins, C. Emmelmann, Process and mechanical properties: applicability of a scandium modified Al-alloy for laser additive manufacturing, Physics Procedia 12 (2011) 369–374.
[2] F. Palm, K. Schmidtke, A.S.M. International, Exceptional grain refinement in directly built up Sc-modified AlMg-alloys is promising a quantum leap in ultimate light weight design, in: International Conference; 9th, Trends in Welding Research, ASM International, Materials Park, OH, Chicago, IL, 2013.

[3] A.B. Spierings, K. Dawson, T. Heeling, P.J. Uggowitzer, et al., Microstructural features of Sc- and Zr-modified Al-Mg alloys processed by selective laser melting, Mater. Des. 115 (2017) 52–63.
[4] A.B. Spierings, K. Dawson, K. Kern, F. Palm, et al., SLM-processed Sc- and Zr-modified Al-Mg alloy: mechanical properties and microstructural effects of heat treatment, Mater. Sci. Eng. 701 (2017) 264–273.
[5] R. Goswami, G. Spanos, P.S. Pao, R.L. Holtz, Precipitation behavior of the ß phase in Al-5083, Mater. Sci. Eng. 527 (4) (2010) 1089–1095.
[6] V.G. Davydov, V.I. Elagin, V.V. Zakharov, D. Rostoval, Alloying aluminum alloys with scandium and zirconium additives, Met. Sci. Heat Treat. 38 (8) (1996) 347–352.
[7] J.L. Murray, The Al-Sc (aluminum-scandium) system, J. Phase Equil. 19 (4) (1998) 380.
[8] J. Røyset, N. Ryum, Scandium in aluminium alloys, Int. Mater. Rev. 50 (1) (2005) 19–44.
[9] V.V. Zakharov, Effect of scandium on the structure and properties of aluminum alloys, Met. Sci. Heat Treat. 45 (7) (2003) 246–253.
[10] C.B. Fuller, J.L. Murray, D.N. Seidman, Temporal evolution of the nanostructure of Al (Sc, Zr) alloys: Part I–Chemical compositions of Al3 (Sc1− xZrx) precipitates, Acta Mater. 53 (20) (2005) 5401–5413.
[11] M. Awd, J. Tenkamp, M. Hirtler, S. Siddique, et al., Comparison of microstructure and mechanical properties of Scalmalloy® produced by selective laser melting and laser metal deposition, Materials 11 (1) (2018).
[12] P. Jakkula, G. Ganzenmüller, F. Gutmann, A. Pfaff, et al., Strain rate sensitivity of the additive manufacturing material Scalmalloy®, Journal of Dynamic Behavior of Materials (2021) 1–8.
[13] M. Muhammad, P.D. Nezhadfar, S. Thompson, A. Saharan, et al., A comparative investigation on the microstructure and mechanical properties of additively manufactured aluminum alloys, Int. J. Fatig. 146 (2021) 106165.
[14] M.O. Lai, W.G. Ferguson, Fracture toughness of aluminium alloy 7075-T6 in the as-cast condition, Mater. Sci. Eng. 74 (2) (1985) 133–138.
[15] T.H. Becker, T.J. Marrow, R.B. Tait, Damage, crack growth and fracture characteristics of nuclear grade graphite using the Double Torsion technique, J. Nucl. Mater. 414 (1) (2011) 32–43.
[16] T.H. Becker, M. Mostafavi, R.B. Tait, T.J. Marrow, An approach to calculate the J-integral by digital image correlation displacement field measurement, Fatig. Fract. Eng. Mater. Struct. 35 (10) (2012) 971–984.
[17] T.V. Hareesh, F.P. Chiang, Integrated experimental-finite element approach for studying elasto-plastic crack-tip fields, Eng. Fract. Mech. 31 (3) (1988) 451–461.
[18] R.M. Pitti, C. Badulescu, M. Grédiac, Characterization of a cracked specimen with full-field measurements: direct determination of the crack tip and energy release rate calculation, Int. J. Fract. 187 (1) (2014) 109–121.
[19] J.P. Isaac, S. Dondeti, H.V. Tippur, Crack initiation and growth in additively printed ABS: effect of print architecture studied using DIC, Additive Manufacturing 36 (2020) 101536.
[20] J.P. Isaac, S. Dondeti, H.V. Tippur, Fracture behavior of additively printed ABS: effects of print architecture and loading rate, Int. J. Solid Struct. 212 (2021) 80–95.
[21] A.T. Owens, H.V. Tippur, Measurement of mixed-mode fracture characteristics of an epoxy-based adhesive using a hybrid digital image correlation (DIC) and finite elements (FE) approach, Opt Laser. Eng. 140 (2021) 106544.
[22] Q. Jia, P. Rometsch, P. Kürnsteiner, Q. Chao, et al., Selective laser melting of a high strength AlMnSc alloy: alloy design and strengthening mechanisms, Acta Mater. 171 (2019) 108–118.
[23] K. Xia, W. Yao, Dynamic rock tests using split Hopkinson (Kolsky) bar system – a review, Journal of Rock Mechanics and Geotechnical Engineering 7 (1) (2015) 27–59.
[24] E.D.H. Davies, S.C. Hunter, The dynamic compression testing of solids by the method of the split Hopkinson pressure bar, J. Mech. Phys. Solid. 11 (3) (1963) 155–179.
[25] T. Nakamura, C.F. Shih, L.B. Freund, Analysis of a dynamically loaded three-point-bend ductile fracture specimen, Eng. Fract. Mech. 25 (3) (1986) 323–339.
[26] S. Griffiths, M.D. Rossell, J. Croteau, N.Q. Vo, et al., Effect of laser rescanning on the grain microstructure of a selective laser melted Al-Mg-Zr alloy, Mater. Char. 143 (2018) 34–42.
[27] K.E. Knipling, D.C. Dunand, D.N. Seidman, Precipitation evolution in Al–Zr and Al–Zr–Ti alloys during isothermal aging at 375–425°C, Acta Mater. 56 (1) (2008) 114–127.
[28] K.E. Knipling, D.C. Dunand, D.N. Seidman, Precipitation evolution in Al–Zr and Al–Zr–Ti alloys during aging at 450–600°C, Acta Mater. 56 (6) (2008) 1182–1195.
[29] S. Costa, H. Puga, J. Barbosa, A.M.P. Pinto, The effect of Sc additions on the microstructure and age hardening behaviour of as cast Al–Sc alloys, Mater. Des. 42 (2012) 347–352.
[30] Y.V. Milman, D.V. Lotsko, O.I. Sirko, Sc effect' of improving mechanical properties in aluminium alloys, Mater. Sci. Forum 331–337 (2000) 1107–1112.